Neurobiology of Disease 175 (2022) 105921

Contents lists available at ScienceDirect

Neurobiology of Disease

journal homepage: www.elsevier.com/locate/ynbdi

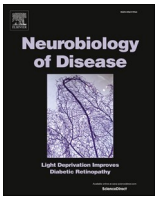

Thioredoxin deficiency increases oxidative stress and causes bilateral symmetrical degeneration in rat midbrain

Iori Ohmori [a,b,*], Mamoru Ouchida [c], Hirohiko Imai [d], Saeko Ishida [e], Shinya Toyokuni [f], Tomoji Mashimo [e]

[a] Section of Developmental Physiology and Pathology, Faculty of Education, Okayama University, Tsushima 3-chome 1-1, Kita-ku, Okayama 700-8530, Japan
[b] Department of Child Neurology, Graduate School of Medicine, Dentistry and Pharmaceutical Sciences, Okayama University, Shikatacho 2-Chome 5-1, Kita-Ku, Okayama 700-8558, Japan
[c] Department of Molecular Oncology, Graduate School of Medicine, Dentistry and Pharmaceutical Sciences, Okayama University, Shikatacho 2-Chome 5-1, Kita-Ku, Okayama 700-8558, Japan
[d] Department of Systems Science, Kyoto University Graduate School of Informatics, Yoshida-Honmachi, Sakyo-ward, Kyoto 606-8501, Japan
[e] Division of Animal Genetics, Laboratory Animal Research Center, Institute of Medical Science, The University of Tokyo, Tokyo 108-8639, Japan
[f] Department of Pathology and Biological Responses, Nagoya University Graduate School of Medicine, 65 Tsurumai-Cho, Showa-Ku, Nagoya 466-8550, Japan

ARTICLE INFO

Keywords:
Txn1
Thioredoxin
Mitochondria
Vacuolar degeneration
Epilepsy
Oxidative stress

ABSTRACT

Thioredoxin, encoded by *Txn1*, acts as a critical antioxidant in the defense against oxidative stress by regulating the dithiol/disulfide balance of interacting proteins. The role of thioredoxin in the central nervous system (CNS) is largely unknown. A phenotype-driven study of *N*-ethyl-*N*-nitrosourea-mutated rats with wild-running seizures revealed the importance of *Txn1* mutations in CNS degeneration. Genetic mapping identified *Txn1*-F54L in the epileptic rats. The insulin-reducing activity of *Txn1*-F54L was approximately one-third of that of the wild-type (WT). Bilateral symmetrical vacuolar degeneration in the midbrain, mainly in the thalamus and the inferior colliculus, was observed in the *Txn1*-F54L rats. The lesions displayed neuronal and oligodendrocytic cell death. Neurons in *Txn1*-F54L rats showed morphological changes in the mitochondria. Vacuolar degeneration peaked at five weeks of age, and spontaneous repair began at seven weeks. The TUNEL assay showed that fibroblasts derived from homozygotes were susceptible to cell death under oxidative stress. In five-week-old WT rats, energy metabolism in the thalamus was significantly higher than that in the cerebral cortex. In conclusion, in juvenile rats, *Txn1* seems to play an essential role in reducing oxidative stress in the midbrains with high energy metabolism.

1. Introduction

Oxidative stress modulates functions ranging from cell homeostasis to cell death (Dröge, 2002). Under physiological conditions, low production of mitochondrial reactive oxygen species (ROS) is required for cellular signaling pathways, such as those regulating proliferation and differentiation. In contrast, excess ROS causes protein denaturation and promotes cell death. The delicate balance between the beneficial and harmful effects of ROS is a vital aspect of living cells and tissues (Dröge, 2002).

The brain is more vulnerable to oxidative stress than other organs. Compared to the liver or kidney, the brain has a higher oxygen

Abbreviations: 4-HNE, 4-hydroxynonenal; 8-OHdG, 8-hydroxy-2′-deoxyguanosine; ALS, amyotrophic lateral sclerosis; CAT, catalase; CNS, central nervous system; DAB, 3,3′-diaminobenzidine; ENU, N-ethyl-N-nitrosourea; GAPDH, Glyceraldehyde 3-phosphate dehydrogenase; GFAP, glial fibrillary acidic protein; GPx, glutathione peroxidase; GSH, Glutathione; HD, Huntington's disease; HE, hematoxylin and eosin; IHC, immunohistochemistry; KB, Klüver-Barrera; MRI, magnetic resonance imaging; MS, multiple sclerosis; NADPH, Nicotinamide adenine dinucleotide phosphate; NOX, NADPH oxidases; PBS, phosphate-buffered saline; Prdx, peroxiredoxin; ROS, reactive oxygen species; SOD, superoxide dismutase; TEM, Transmission electron microscope; TUNEL, Terminal deoxynucleotidyl transferase-mediated dUTP Nick End Labeling; Txn, thioredoxin; WT, wild type..

* Corresponding author at: Section of Developmental Physiology and Pathology, Faculty of Education, Okayama University, Tsushima 3-chome 1-1, Kita-ku, Okayama 700-8530, Japan.

E-mail addresses: iori@md.okayama-u.ac.jp (I. Ohmori), ouchidam@md.okayama-u.ac.jp (M. Ouchida), imai@sys.i.kyoto-u.ac.jp (H. Imai), saeishida@ims.u-tokyo.ac.jp (S. Ishida), toyokuni@med.nagoya-u.ac.jp (S. Toyokuni), mashimo@ims.u-tokyo.ac.jp (T. Mashimo).

https://doi.org/10.1016/j.nbd.2022.105921
Received 3 May 2022; Received in revised form 26 October 2022; Accepted 7 November 2022
Available online 11 November 2022

consumption, in some areas has an increased iron content that catalyzes the generation of ROS, has elevated amounts of lipids with unsaturated fatty acids, and has lower activities of superoxide dismutase (SOD), catalase (CAT), and glutathione peroxidase (GPx) (Dringen, 2000). Several studies have established a link between oxidative stress and neurodegenerative diseases such as Alzheimer's disease, Parkinson's disease, Huntington's disease (HD), amyotrophic lateral sclerosis (ALS), and multiple sclerosis (MS) (Elfawy and Das, 2019; Lin and Beal, 2006; Uttara et al., 2009). In addition, animal models and clinical studies suggest that disruption of redox homeostasis may contribute to the etiology of psychological disorders (Ng et al., 2008), including anxiety (Hovatta et al., 2005), major depression (Eren et al., 2007; Forlenza and Miller, 2006), and schizophrenia (Gysin et al., 2007; Saadat et al., 2007).

The primary endogenous sources of ROS in mammals, including humans, are the mitochondrial respiratory chain and NADPH oxidases (NOX). (Dan Dunn et al., 2015; Nathan and Cunningham-Bussel, 2013; Sarniak et al., 2016). Living organisms have a defense system that scavenges ROS produced by mitochondria. The enzymatic antioxidant system consists of SOD, CAT, GPx, and thioredoxin. Thioredoxin was first identified as a hydrogen donor for ribonucleotide reductase in *Escherichia coli* (Laurent et al., 1964). In humans, thioredoxin has been identified in the culture media of adult T-cell leukemia cell lines and Epstein-Barr virus-infected cells (Wakasugi et al., 1990). Subsequently, it has been reported that thioredoxin expression is upregulated in many cancer cells and that it inhibits cancer cell apoptosis (Baker et al., 1997; Lincoln et al., 2003). However, few studies have investigated the role of the thioredoxin system in vivo. Homozygous *Txn1* knockout mice are embryonically lethal, whereas heterozygous mice show normal development (Matsui et al., 1996). A previous study reported that transgenic mice overexpressing a dominant-negative mutant of *Txn1* show cardiac hypertrophy (Yamamoto et al., 2003). Little is known about the effects of reduced thioredoxin activity in vivo.

We recently discovered a strain, from the Kyoto University archive, that harbors chemically induced *Txn1* mutation in rats with running seizures. This study aimed to identify the causative genes for running seizures and elucidate the neuropathology of this rat strain. Here, we present a novel animal model for neurodegeneration designated as *Adem* "Age-dependent mitochondrial cytopathy" rat.

2. Materials and methods

2.1. Animals

We used *Txn1*-F54L rats (*Adem*) generated by ENU-mutagenesis and a *Txn1*- T160C (p. F54L) knock-in rat generated by CRISPR-Cas 9. We used the former for the identification of the causative gene and its characterization. The latter was created to confirm the reproducibility of the phenotype. The *Txn1*-F54L rat was initially discovered in an ENU-induced mutant archive at Kyoto University (Mashimo et al., 2008; Serikawa et al., 2009) as a rare strain with frequent running seizures only in its juvenile stage. All animal husbandry procedures were performed in accordance with the protocols approved by the institutional experimental animal use committees Okayama University, Osaka University, and Kyoto University. Both sexes were used in the present study, as there was no difference in the frequency of running seizures. Number of rats used in experiments were summarized in Supplementary Table 1.

2.2. Genetic mapping and sequencing analysis of the Adem rat generated by ENU-mutagenesis

The rats with running seizures were backcrossed for more than ten generations on the *F344/NSlc* inbred background (Japan SLC, Hamamatsu, Japan). The repeated backcrosses ensure that the frequency of potential mutations induced by ENU elsewhere in the genome is reduced to approximately 1 in 4×10^6 bp of the genome. To identify the causative gene, we produced 117 (*Adem*×*BN/SsNSlc*) × *BN/SsNSlc* backcross progeny. Genetic locus mapping was determined in rats with wild running or generalized tonic-clonic seizure phenotypes. Genomic DNA was extracted from rat tail biopsies by an automatic genomic DNA isolation system (PI-200; Kurabo, Osaka, Japan). To localize the locus to a specific chromosomal region, genome-wide scanning on DNA samples was performed using simple sequence length polymorphism (SSLP) markers covering all autosomal chromosomes (Chrs) as previously reported (Ishida et al., 2012).

To enrich the 1.5-Mb region (Chr 5: 75,159,000 to 76,708,000), SureSelect custom DNA probes were designed by SureDesign under moderately stringent conditions and generated by Agilent Technologies (Santa Clara, CA, USA). The DNA library was prepared using SureSelect reagents and a custom probe kit. Genomic sequence analysis was performed by HiSeq 2500 (2 × 150 bp) in accordance with the standard protocol at Takara Bio (Takara Bio Inc., Shiga, Japan).

2.3. Generation of Txn1- T160C (p. F54L) knock-in rat using CRISPR-Cas 9

The possibility of genomic DNA alterations around the *Txn1* gene could not be fully excluded in *Txn1*-F54L rats generated by ENU mutagenesis. As the *Txn1* mutant rats showed a unique phenotype never reported previously, we generated a new *Txn1*-F54L knock-in rat to test the reproducibility of this phenotype. A *Txn1* T160C (p. F54L) knock-in rat was generated by CRISPR-Cas9 genome editing with long single-stranded DNA (lssDNA), as previously reported (Yoshimi et al., 2016). A pair of guide RNAs (gRNAs) targeting intron 1 and intron 2 of rat *Txn1* were designed. LssDNA for *Txn1* was synthesized using a long ssDNA Preparation Kit (Biodynamics Laboratory Inc., Tokyo, Japan) following the manufacturer's protocol. The sequences of gRNA and ssDNA are listed in Supplementary Table 2. Cas9 mRNA (400 ng/μL), gRNA (200 ng/μL), and ssDNA (40 ng/μL) were delivered into 113 *F344/Jcl* embryos by electroporation as previously reported (Miyasaka et al., 2018). The two-cell stage embryos ($n = 110$) were transferred into the oviducts of five pseudopregnant females. Genomic DNA from founder rats was extracted from the tail biopsies. The CRISPR target site was amplified using the specific primer pairs listed in Supplementary Table 2.

2.4. Genotyping

The last 3 mm of the rat tail was cut at three weeks of age, and DNA was purified with a DNeasy Blood &Tissue kit (Qiagen, Hilden, Germany). A DNA fragment containing a mutation was amplified with a pair of primers as follows: FW 5′ - CCA CAT GGG AGA GTC ACA T − 3′ and RV 5′- ATA GCC TGG AAG CGG TCA GAT G − 3′ (Sigma-Aldrich Japan, Inc., Tokyo, Japan). The PCR products (521 bp) were then treated with the restriction enzyme *Bsp*1286I (New England Biolabs, Ipswich, MA, USA), and the F54L mutant DNA was digested to 260 bp and 261 bp fragments. Genotyping was determined by the size of the digested fragments on a 3% agarose gel.

2.5. Video monitoring of wild running

To find the frequency of wild running and subsequent tonic-clonic seizures, both the heterozygotes ($n = 8$, including four males and four females) and homozygotes ($n = 9$, including five males and four females) were placed under a 24-h video monitoring system (Handycam HDR-CX480, SONY, Tokyo, Japan), every week, from three to nine weeks.

2.6. Histological analysis

The brains from both sexes were fixed with 10% formalin neutral buffer solution. Tissue sections were cut from paraffin-embedded brain samples taken at 2, 3, 5, and 9 weeks of age and were subjected to hematoxylin and eosin (HE) and Bodian and Klüver-Barrera (KB) staining using standard protocols. We used 31 rats for WT, 37 for heterozygotes,

and 33 for homozygotes to confirm the histological changes. The stained sections were examined under a BZX-700 microscope (Keyence, Osaka, Japan). We evaluated brain lesions, including samples from the thalamus and the inferior colliculus, in the sagittal and coronal planes.

2.7. Head MRI

To evaluate the extent of brain lesions and their changes over time, an MRI scan was performed in 1-mm slices. Three animals were examined for each genotype at 5, 7, and 9 weeks of age. The same animal was examined twice on days 1 and 14 as the storage period of the MRI-attached breeding room was limited to no longer than two weeks. The rats were anesthetized with isoflurane and laid prone on a cradle. Anesthesia was maintained by inhalation of 2% isoflurane in the air at 1.4 L/min through a face mask. Throughout the MRI measurements, respiratory rate and rectal temperature were monitored using a dedicated system (Model 1025, MR-compatible Small Animal Monitoring and Gating System, SA Instruments, Inc., Stony Brook, NY, USA). The body temperature was maintained by a flow of warm air using a heater system (MR-compatible Small Animal Heating System, SA Instruments).

All MR images were obtained with a 4.7 Tesla preclinical MR scanner (BioSpec 47/16 USR, Bruker BioSpin MRI GmbH, Ettlingen, Germany). A quadrature volume resonator (Bruker BioSpin) was used for signal detection. The scanner was operated using ParaVision 6.0.1 (Bruker BioSpin). Two-dimensional multi-slice T2-weighted MR imaging was performed using a rapid acquisition with relaxation enhancement (RARE) sequence. The whole-head images were acquired in three orthogonal (coronal, sagittal, and axial) orientations. The acquisition parameters were as follows: echo time (TE), 12 ms; effective TE, 36 ms; RARE factor, 8; acquisition bandwidth, 62.5 kHz; in-plane spatial resolution, 0.156×0.156 mm^2; slice thickness, 1 mm; slice gaps, 0 mm; the number of averages, 2. For coronal orientation, repetition time (TR), 3000 ms; field of view (FOV), 25×29.3 mm^2, matrix size, 120×136 (zero-filled to 160×188 before image reconstruction); the number of slices, 24; acquisition time, 1 min 42 s. For sagittal orientation, TR, 2500 ms; FOV, 27×27.5 mm^2, matrix size, 131×128 (zero-filled to 173×176); the number of slices, 18; acquisition time, 1 min 20 s. For axial orientation, TR, 2500 ms; FOV, 27×30.5 mm^2, matrix size, 131×144 (zero-filled to 173×195); the number of slices, 16; acquisition time, 1 min 30 s.

2.8. Western blotting

Western blotting was used to quantify the thioredoxin expression levels in multiple organs in rats. Proteins were extracted from four rats of both sexes per phenotype and age. Protein concentration was measured using an assay kit (Pierce™ BCA Protein Assay Kit, ThermoFisher Scientific, Waltham, MA, USA) and adjusted to 2 μg/μl. The protein extracts (10 μg) were mixed with a sample buffer solution (Nakalai Tesque, Kyoto, Japan), denatured at 95 °C for 5 min, and loaded onto a sodium dodecyl sulfate (SDS)-polyacrylamide gel (Mini-protean TGX Precast gels; Bio-Rad, Hercules, CA) for electrophoresis. The proteins were blotted onto a polyvinylidene fluoride (PVDF) membrane using the iBlot Dry Blotting System (ThermoFisher Scientific, Waltham, MA, USA). Membranes were incubated with anti-Thioredoxin1 rabbit antibody (CST#2298; Cell Signaling Technology, Danvers, MA, USA), anti-NeuN rabbit antibody (ab177487; Abcam, Cambridge, UK), anti-Olig2 rabbit antibody (ab109186; Abcam), anti-glial fibrillary acidic protein (GFAP) rabbit antibody (ab7260; Abcam), anti-Iba1 rabbit antibody (ab178847; Abcam), and anti-glyceraldehyde 3-phosphate dehydrogenase (GAPDH) rabbit antibody (CST #2118). Mouse and rabbit primary antibodies were detected using anti-mouse IgG-HRP-linked antibody (CST #7076) and anti-rabbit IgG-HRP-linked antibody (CST; #7074), respectively. Chemiluminescence was detected using Western Lightning ECL Pro (PerkinElmer Japan, Kanagawa, Japan) and the ChemiDoc Touch (Bio-Rad).

2.9. Immunohistochemistry (IHC) analyses

A standard IHC protocol was used to stain the brain tissue samples ($n = 5$ or 6 rats per genotype). Each phenotype included both sexes. The individual rats used in IHC were the same as those used in histological analysis. In brief, 5-μm-sized paraffin-embedded tissue sections were deparaffinized with xylene. Antigen retrieval was performed by autoclaving at 120 °C for 5 min. Endogenous peroxidases were quenched by treatment with 0.3% hydrogen peroxide (H_2O_2) in methanol for 30 min at 22–26 °C. They were then incubated with blocking serum for 1 h at 22–26 °C. Sections were incubated with the following primary antibodies to determine the cell type in the brain lesion: anti-NeuN rabbit antibody (ab177487; Abcam) and anti-Olig2 rabbit antibody (ab109186; Abcam) for 1 h at room temperature. To determine DNA oxidative injury and lipid peroxidation, sections were stained with anti-8-hydroxy-2′-deoxyguanosine (8-OHdG) mouse antibody (MOG-020P, JaICA, Tokyo, Japan), and anti-4-hydroxynonenal (4-HNE) mouse antibody (MHN-020P, JaICA) overnight at 4 °C, respectively. The sections were then reacted with a biotinylated rabbit polyclonal secondary antibody (PK-6200, Vector Laboratories, Burlingame, CA, USA). To reveal the staining, we used an avidin-biotinylated peroxidase complex (PK-6200, Vector Laboratories). After washing, the slides were incubated with 3,3′-diaminobenzidine (DAB) (SK-4100, Vector Laboratories) and immediately washed with tap water after colour development. The slides were then counterstained with hematoxylin, mounted with dibutyl phthalate xylene (DPX), and observed under a BZX-700 multifunctional microscope (Keyence). IHC was quantified by assessing five randomly selected fields in the inferior colliculus and thalamus. The percentages of positive cells or positive areas were calculated using the BZX Analyzer software (Keyence).

2.10. Transmission electron microscopy (TEM)

Six brain samples per genotype were obtained and further immersed in 2% glutaraldehyde and 2% paraformaldehyde in 100 mM phosphate buffer (PB) for 24 h at 4 °C. They were then postfixed with 2% osmium tetroxide in 100 mM PB for 1.5 h at 4 °C, after which they were rinsed with 100 mM PB, and dehydrated through a graded series of ethanol treatments. They were embedded in Spurr resin (Polysciences Inc., Warrington, PA, USA), cut into ultrathin sections, and stained with uranyl acetate and lead citrate. The ultrathin sections were observed using a Hitachi H-7650 TEM (Hitachi High-Tech Corp., Tokyo, Japan).

2.11. Plasmids and purification of recombinant proteins

For recombinant Thiredoxin1 proteins, rat *Txn1* cDNAs were amplified by PCR using LA-Taq polymerase (Takara Bio) with FW-primer: 5′-GGA TCC ATG GTG AAG CTG ATC GAG AG-3′; and RV-primer, 5′- GTC GAC TTA GCT GTC CAT GTG CTG GCG TTC GAA TTT AGC GGT TTC TTT GAA TTC GGC AAA CTC CGT AAT AGT GG-3′ (Sigma-Aldrich Japan). *Txn1* C35S mutation was introduced by PCR with C35S-FW 5′- GTG GAC CTA GCA AAA TGA TCA AG-3′ and C35S-RV 5′- TGA TCA TTT TGC TAG GTC CAC AC-3′. The PCR products were cloned into a pCMV-Tag2 plasmid (Stratagene, San Diego, CA, USA) digested with *Bam*HI and *Sal*I containing FLAG-tag and S-tag sequences. The DNA sequence of the plasmids was confirmed by DNA sequencing using a BigDye Terminator FS Ready-Reaction Kit (Applied Biosciences, Little Chalfont, Buckinghamshire, UK) and an ABI 3130× Genetic Analyzer (Applied Biosciences). The plasmids with two clones per genotype were cloned into DH5α competent cells and purified with a Plasmid DNA purification kit (Qiagen 12,145) after being cultured overnight. The plasmids were transfected into HEK293 human embryonic kidney cells using Lipofectamine2000 (Invitrogen, Carlsbad, CA, USA). The recombinant proteins were purified with anti-FLAG agarose affinity gel (A2220; Sigma-Aldrich Japan), eluted with FLAG peptide (A3290; Sigma-Aldrich Japan), and filtered using an ultrafiltration

membrane (Amicon Ultra 3 K; Millipore, Burlington, MA, USA).

2.12. Insulin-reducing activity assay

Thioredoxin activity was measured thrice using a thioredoxin activity assay kit (Redoxica, Little Rock, AR, USA) according to the manufacturer's instructions. We used two clones per genotype for recombinant assay and three rats, including both sexes, for brain tissue assay. In brief, the purified recombinant thioredoxin1 proteins or protein extracts from rat thalamus and cortex were allowed to react with insulin and NADPH in assay buffer, and thioredoxin activity was determined as the change in the amount of oxidized NADPH by measuring the decrease in absorbance at 340 nm per minute using a spectrophotometer DeNovix DS-11 (DeNovix, Tokyo, Japan).

2.13. Assay of oxidative stress in the midbrain lesions

We measured cellular H_2O_2 concentration of the midbrain in WT and heterozygotes ($n = 8$, including two males and two females for each hemisphere) at five weeks using a colorimetric H_2O_2 assay kit (no. STA-844, Cell Biolabs, San Diego, USA) according to the manufacturer's protocol.

2.14. Primary fibroblast culture

Newborn rats ($n = 4$ per genotype) were sacrificed under deep anesthesia with isoflurane on the day of birth. The animals were dissected in the surgical suite and disinfected with 70% alcohol. For primary fibroblast culture, the abdominal skin tissues were cut into small pieces in DMEM (Fujifilm Wako Pure Chemical Corporation, Osaka, Japan) and disrupted by pipetting. The cell suspension was transferred and maintained in DMEM supplemented with 10% fetal bovine serum (Thermo Fisher Scientific), 500 U/mL penicillin, and 500 μg/mL streptomycin (Sigma-Aldrich Japan) in a fully humidified atmosphere of 5% CO_2. After about two weeks, fibroblast cells were cultured in DMEM supplemented with 10% fetal bovine serum, 100 U/mL penicillin, and 100 μg/mL streptomycin.

2.15. Terminal deoxynucleotidyl transferase (TdT) dUTP Nick-End Labeling (TUNEL) assay

For determining apoptosis, primary fibroblasts derived from a total of four rats were assessed twice using the In Situ Cell Death Detection Kit TMR red (Sigma-Aldrich Japan) following the manufacturer's instructions. We compared cell death during incubation of primary fibroblasts with and without the addition of 300 μM H_2O_2 for 3 h. In brief, the cells were cultured on an 8-chamber culture slide (BD Falcon, Franklin Lakes, NJ, USA), washed with phosphate-buffered saline (PBS), fixed with 10% formalin neutral buffer solution (Fujifilm Wako Pure Chemical Corporation) for 1 h at room temperature, and treated with permeabilization solution for 2 min on ice. TMR red-labeled dUTP was incorporated into 3′-OH DNA ends by terminal deoxynucleotidyl transferase, and the fluorescence signal was detected using a BZX-700 microscope (Keyence) or a fluorescence microscope (Olympus IX71; Olympus Corporation, Tokyo, Japan).

2.16. Metabolite measurements in the brain

We considered the possibility that localization-specific metabolic differences in the midbrain might be related to neurodegeneration. Vacuolar degeneration occurs in the midbrains in both heterozygotes and homozygotes, but the lesion area is narrower in the heterozygotes. While removing brain tissue from gross anatomy, samples from heterozygotes may contain areas that lacked vacuolar degeneration. Thus, we compared metabolite differences between the thalamus and cerebral cortex in WT and homozygous rats (each $n = 3$). First, 5-week-old rats were anesthetized deeply enough with isoflurane and decapitated after whole blood collection. Then, the removed midbrain samples were immediately frozen with liquid nitrogen and stored in a − 80 °C freezer. The temperature was strictly controlled in a cold box with dry ice while sending the samples to the Human Metabolome Technologies (HMT) company for analysis. The analysis of 116 hydrophilic and ionic metabolites involved in central energy metabolism pathways (glycolysis, TCA cycle, amino acid metabolism, and nucleic acid metabolism) was done. Capillary electrophoresis time-of-flight mass spectrometry (CE-TOFMS) and CE-tandem mass spectrometry (CE-MS/MS) analysis were carried out using an Agilent CE capillary electrophoresis system equipped with an Agilent 6210 time-of-flight mass spectrometer (Agilent Technologies) and Agilent 6460 Triple Quadrupole LC/MS (Agilent Technologies), respectively. The systems were controlled by Agilent G2201AA ChemStation software version B.03.01 for CE (Agilent Technologies) and connected by a fused silica capillary (50 μm *i.d.* × 80 cm total length) with commercial electrophoresis buffer (H3301–1001 and I3302–1023 for cation and anion analyses, respectively, HMT) as the electrolyte. The time-of-flight mass spectrometer was scanned from m/z 50 to 1000 (Ohashi et al., 2008), and the triple quadrupole mass spectrometer was used to detect compounds in dynamic MRM mode. Peaks were extracted using MasterHands, automatic integration software (Keio University, Tsuruoka, Yamagata, Japan) (Sugimoto et al., 2010), and MassHunter Quantitative Analysis B.04.00 (Agilent Technologies) in order to obtain peak information, including m/z peak area, and migration time (MT).

2.17. Statistical analysis

Results are expressed as the mean ± SEM. All data were analyzed using the EZR software (Kanda, 2013). Welch's *t*-test was used for comparisons between two groups. One-way analysis of variance (ANOVA) was used to compare three groups. Statistical significance was set at $p < 0.05$. Bonferroni adjustment was used to determine the statistical differences between three groups. All significant statistical results are indicated within the figures using the following conventions: * $p < 0.05$, ** $p < 0.01$, *** $p < 0.001$.

2.18. Theory/Calculation

For metabolite analysis, hierarchical cluster analysis (HCA) and principal component analysis (PCA) (Yamamoto et al., 2014) were performed using HMT's proprietary MATLAB and R programs, respectively.

3. Results

3.1. Discovery of a novel epileptic rat with Txn1 missense mutation

A strain exhibiting unique running seizures was identified in an archive of ENU-mutated rats. Here, we identified the responsible gene by analyzing simple sequence length polymorphism (SSLP) markers on mutant ($n = 21$) and sibling ($n = 25$) DNA pools. The *Adem* locus was roughly mapped on chromosomes 2 and 5. The locus was subsequently refined by 26 and 33 SSLP markers for each chromosome and mapped to a 1.5-Mb genomic region between markers D5Mit17 (Chr 5: 75,159,412–75,159,546) and D5Rat113 (Chr 5:76,707,365–76,707,563) (RGSC_v3.4) (Fig. 1a). The *Adem* region has ten known or predicted genes (*Ptpn3*, *Palm2*, *AC134204.1*, *Akap2*, *LOC685849*, *Txn1*, *Txndc8*, *Svep1*, *Musk*, *Lpar1*) were identified from the Ensembl database (http://www.ensembl.org).

We performed next-generation sequencing analysis of genomic DNA from 75,159,000 to 76,708,000 on Chr5 using the SureSelect target enrichment approach (Agilent). In mutant DNA, we found only one heterozygous missense mutation in the exon region, c. T160C, in exon 3 of the *Txn1* gene (NM_053800, ENSRNOG00000012081.6) by

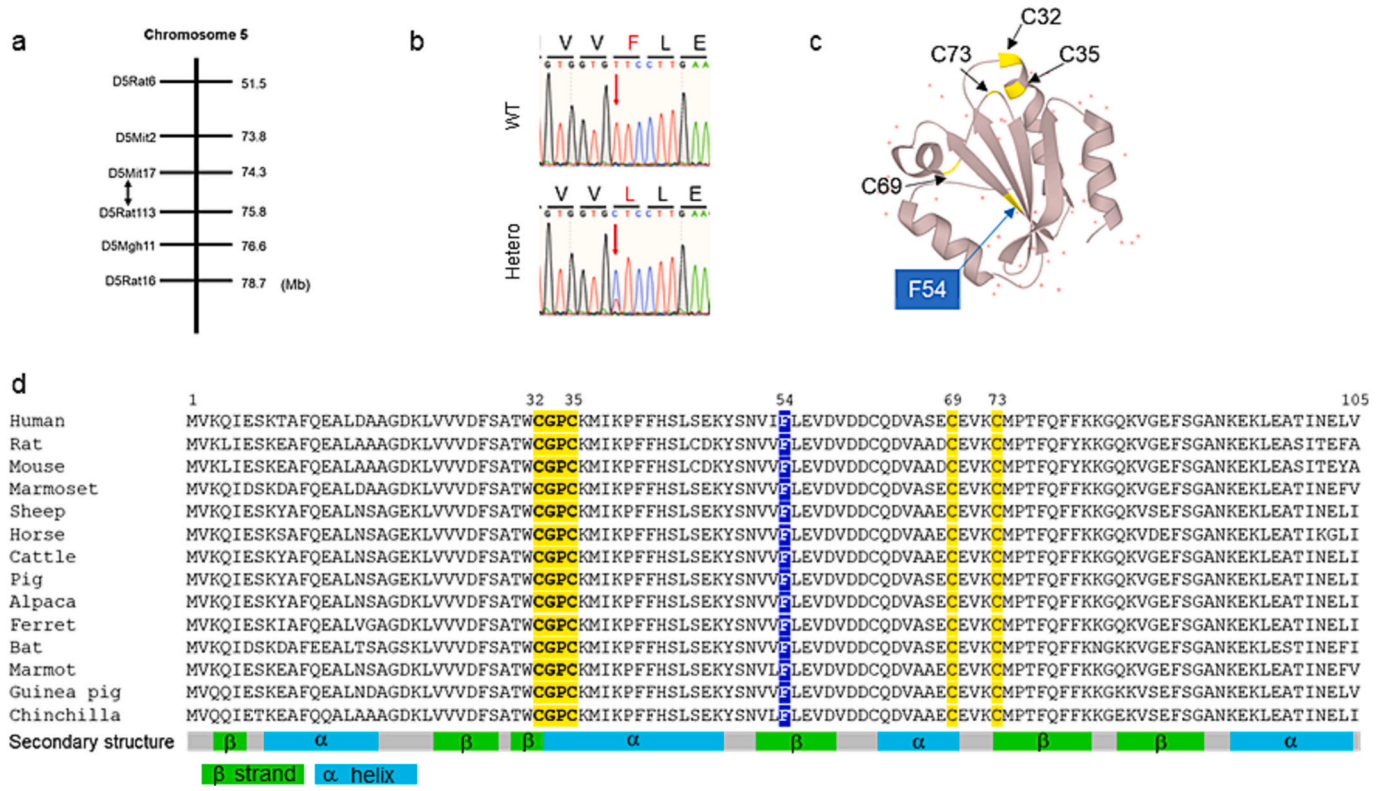

Fig. 1. Discovery of a novel epileptic rat with a *Txn1* missense mutation.
(a) *Adem* locus mapped to a 1.5-Mb genomic region, between markers D5Mit17 and D5Rat113.
(b) DNA sequencing exhibiting c. T160C in exon 3 of the *Txn1* gene, causing a substitution of phenylalanine for leucine at residue 54.
(c) Functional sites and F54 were plotted in the 3D structure of human thioredoxin.
(d) Alignments of the sequence of Txn1 gene in mammals.

comparing the parental strain F344/NSlc. This variant caused a substitution of phenylalanine for leucine at residue 54 (Fig. 1b).

Thioredoxin is widespread in prokaryotes and eukaryotes, and its amino acid sequence is well conserved in mammals (Fig. 1d). Amino acid sequences are 90% identical in humans and rats. Since the structure of rat thioredoxin has not been reported, we plotted the position of F54 on the 3D structure of human thioredoxin (UniProt, https://www.uniprot.org/). The positions of amino acids with important functions in thioredoxin were plotted on the structure. Thioredoxin has an active center sequence Cys32-Gly-Pro-Cys35 motif and carries out redox reactions by dithiol/disulfide exchange reactions between Cys32 and Cys35 (Hirota et al., 1997; Kang et al., 2019; Lu and Holmgren, 2014). Both Cys69 and Cys73 are nitrosylated in response to nitric oxide (NO) (Hirota et al., 1997; Kang et al., 2019). Cys-73 can serve as a donor for the nitrosylation of target proteins. The location of the F54L mutation is remote from these active sites (Fig. 1c and Fig. 1d), suggesting that it is not directly involved in the dithiol/disulfide exchange reaction or S-nitrosylation. However, the PolyPhen-2 prediction (http://genetics.bwh.harvard.edu/pph2/index.shtml) found that the F54L mutation is possibly damaging with a score of 0.785, and the Sorting Intolerant From Tolerant (SIFT, http://www.ngrl.org.uk/Manchester/page/sift-sorting-intolerant-tolerant.html) sequence is deleterious.

3.2. Vacuolar degeneration appears during an epileptic period

Video monitoring showed that the frequency of seizures peaks at five weeks of age in both heterozygotes (Fig. 2a) and homozygotes (Fig. 2b). There were no differences in seizure frequencies between heterozygotes and homozygotes.

Next, a histological examination was performed at five weeks to determine whether a structural change was the cause of epilepsy. Surprisingly, vacuolar degeneration was found in the inferior colliculus and thalamus of the mutants. (Fig. 2c). No changes were observed in the hippocampus, which is prone to epilepsy. Bodian staining, which is used to observe nerve fibers, and Klüver-Barrera (KB) staining, which is used to observe the myelin sheath, exhibited decreased staining in the mutants. These histological tests showed that homozygotes had more severe lesions than heterozygotes. We examined when these lesions had started developing (Fig. 2d). There were no remarkable changes in the inferior colliculus at two weeks of age. However, vacuoles became evident in the inferior colliculus and thalamus at three weeks of age and were widespread at five weeks. They almost disappeared entirely after nine weeks. All rats showed similar changes to the representative findings in Fig. 2c and d, with no exceptions.

3.3. MRI showed transient high signals of T2-weighted images in the midbrain

MRI detected hyperintense regions of T2-weighted images (T2WI) spread around the thalamus in mutant rats at five weeks of age (Fig. 3a). The hyperintense regions of the heterozygous and homozygous T2WI were symmetrical. The lesions were localized in the thalamus, inferior colliculus, superior colliculus, and hypothalamus in homozygotes (Fig. 3b). The hyperintensity region of T2WI in homozygous rats was wider than that in heterozygous rats (see also Supplementary Fig. S1, S2, and S3). Temporal lesions were also examined using MRI in the same individual. Serial MRI examination revealed that the lesions at three weeks spread or were similar in size at five weeks. However, the lesions shrank at seven weeks and disappeared at nine weeks (Fig. 3c). The weekly changes observed on MRI were similar to those seen in the histological examination.

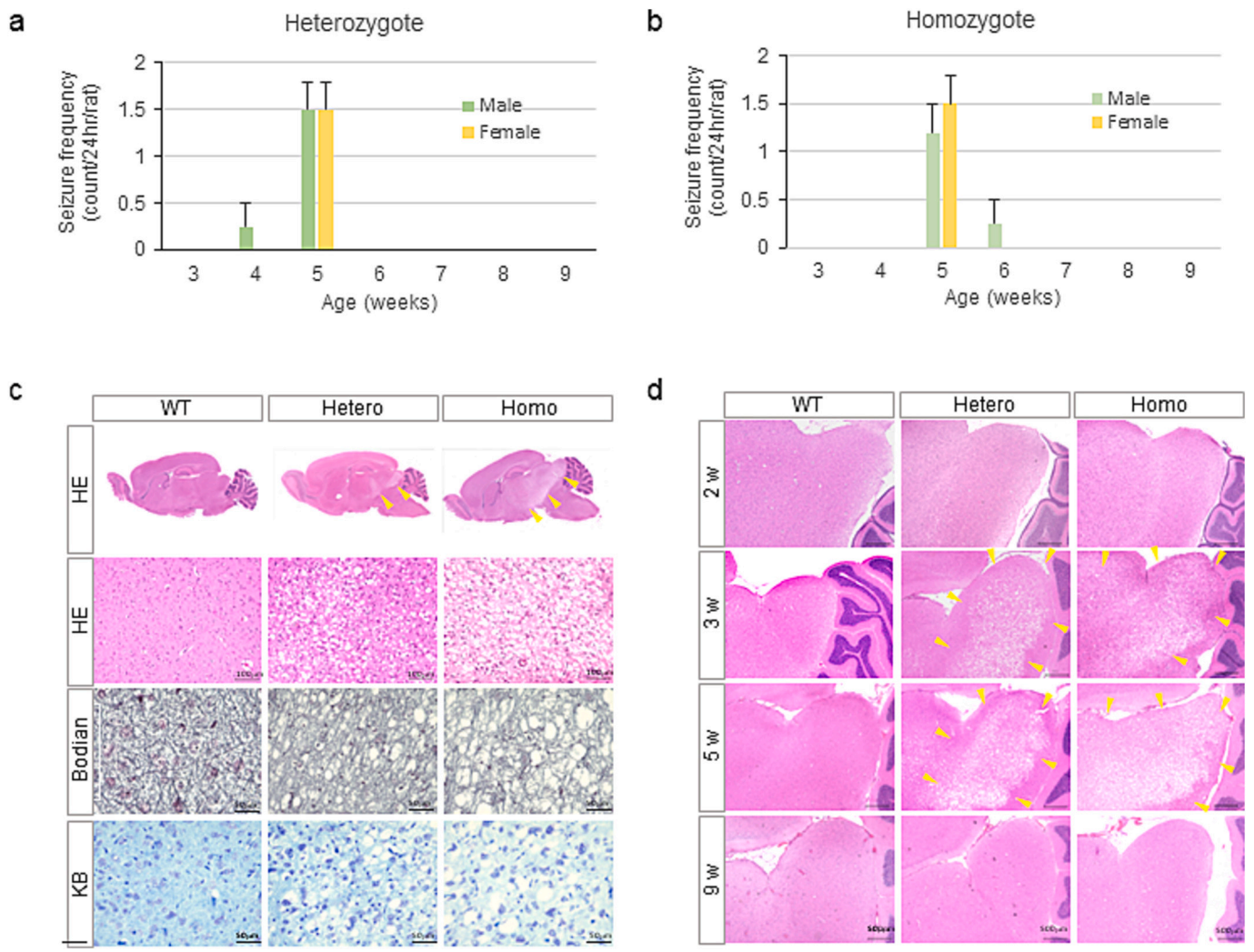

Fig. 2. Vacuolar degeneration appears during an epileptic period.
(a) Seizure frequency of heterozygotes each week/rat ($n = 8$, including four males and four females).
(b) Seizure frequency of homozygotes each week/rat ($n = 9$, including five males and four females).
(c) Histology at five weeks of age. At least four animals of each genotype were examined.
(d) The representative changes of inferior colliculus lesions from 2 to 9 weeks of age for each genotype.

3.4. Neuronal and oligodendrocytic cell loss occurs in the midbrain

Western blotting of the midbrain using NeuN, Olig2, GFAP, and anti-IbaI antibodies showed a decrease in NeuN and Olig2 and an increase in GFAP and IbaI expression in heterozygotes and homozygotes (Fig. 4a). Immunohistochemical studies showed significantly decreased numbers of NeuN-positive neurons (Fig. 4b and c) and Olig2-positive oligodendrocytes (Fig. 4d and e). NeuN-positive neurons in heterozygotes and homozygotes had larger cell bodies than wild-type (WT) rats. Electron microscopy of the lesions in the mutant rats revealed that microtubules in the vacuoles and myelin sheath were wrapped around the vacuoles (Fig. 4h and i). These findings indicate that the vacuoles were dilated axons of the neurons. Examination of the mitochondrial morphology showed sparse cristae in the mutant, even though the neurons retained their structures (Fig. 4j and k).

3.5. Txn1-F54L shows decreased insulin-reducing activity

Fig. 5a shows the thioredoxin/peroxiredoxin system. Four central enzyme systems defend against oxidative stress by scavenging ROS generated in the body. These include SOD, which scavenges superoxide, CAT, GPx, and thioredoxin-dependent peroxiredoxin (Prdx). Thioredoxin forms a system with nicotinamide adenine dinucleotide phosphate (NADPH) and thioredoxin reductase (Txnrd) to reduce disulfide bonds in target proteins. Thioredoxin is responsible for converting the target protein from oxidized to the reduced form and scavenging H_2O_2 via Prdx. H_2O_2 concentration, an important marker of oxidative stress, in the midbrain was significantly higher ($p = 0.01$) in the heterozygotes than in the WT (Fig. 5b). To confirm whether the reduced expression of thioredoxin underlies the changes in the brain during 3–5 weeks of age, we examined the expression level of thioredoxin protein in the brain, kidney, heart, and liver by western blotting at four weeks of age when vacuoles appeared and at 16 weeks of age when repair occurred. We found that *Txn1* was equally expressed in all organs, and there was no change between 4 and 16 weeks of age (Fig. 5f).

Next, we measured thioredoxin activity by using recombinant protein (Fig. 5c), the thalamus at five weeks of age, where vacuolar degeneration was observed (Fig. 5d), and the frontal cortex (Fig. 5e), where vacuolar degeneration did not occur. Our results showed that the insulin-reducing activity of *Txn1*-F54L was decreased to approximately one-third of that of the WT. Similarly, insulin-reduction activity in the thalamus was low in heterozygotes and even lower further in homozygotes compared to WT rats (Fig. 5d). Interestingly, reduced activity was

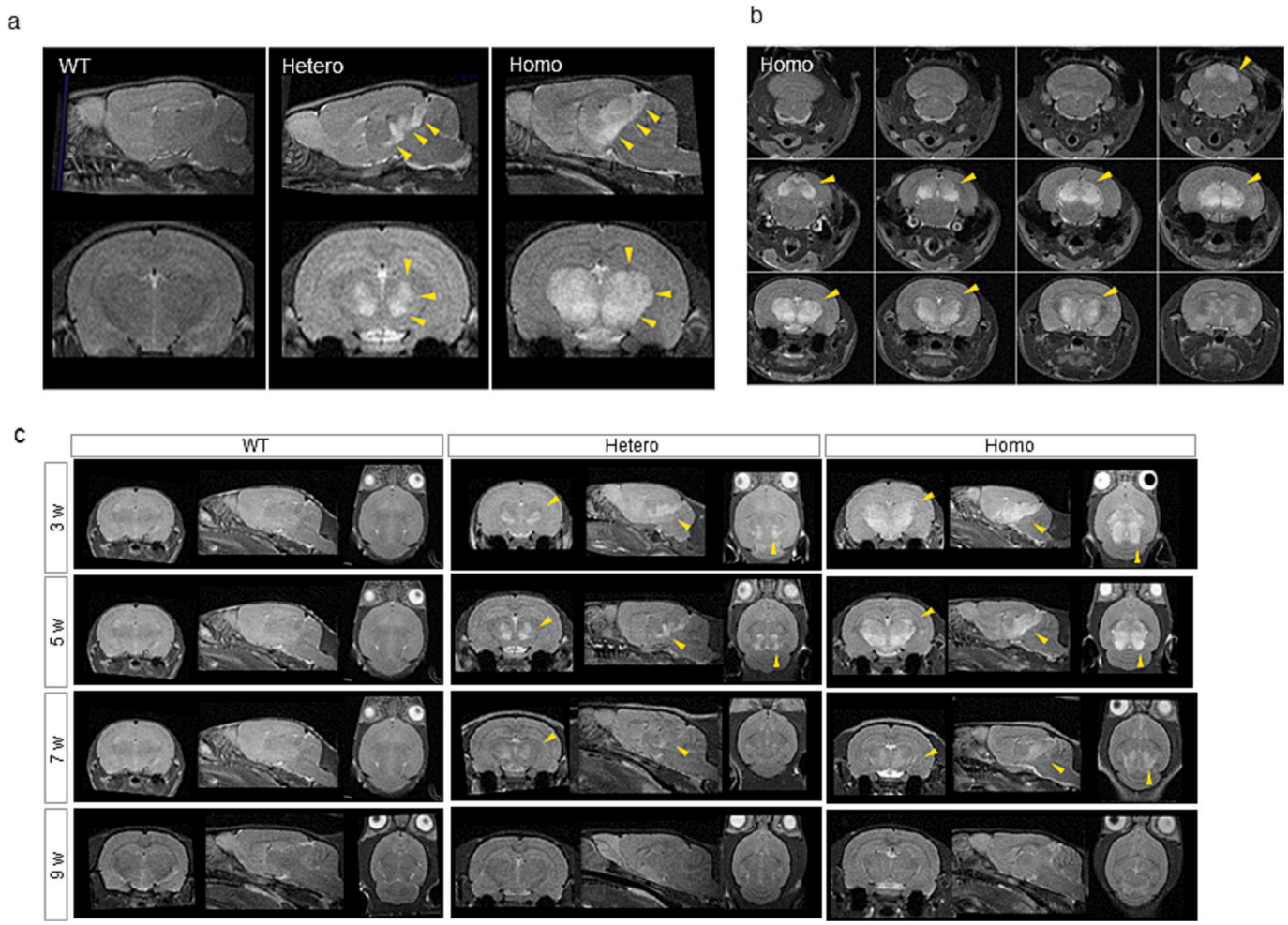

Fig. 3. MRI demonstrates transient high signals of T2-weighted images in the midbrain.
(a) The representative MRI findings at five weeks for each genotype (sagittal slices).
(b) The coronal slices of homozygotes at five weeks.
(c) The temporal changes of the brain lesion for each genotype from three to nine weeks.

also observed in the cortex, where there was no vacuolar degeneration (Fig. 5e).

3.6. Oxidative damage in the midbrain and susceptibility to cell death under oxidative stress

Next, we investigated the pathogenesis underlying vacuolar degeneration. Staining with 8-OHdG, which indicates oxidative stress-induced DNA damage, and 4-HNE, which indicates lipid oxidation, showed brain staining in the mutant lesions (Fig. 6a). The area of 8-OHdG (Fig. 6b) and 4-HNE (Fig. 6c) positive cells were significantly increased in heterozygous and homozygous rats compared to WT cells. Next, we examined cellular vulnerability to H_2O_2 using primary fibroblasts derived from WT and homozygous rats. The TUNEL assay showed that homozygous fibroblasts were slightly stained even under a standard culture medium, and the staining became significantly stronger when H_2O_2 was added. In contrast, TUNEL-positive cells in WT fibroblasts did not increase with the addition of 0.3 mM H_2O_2 (Fig. 6d).

3.7. WT energy metabolism in the thalamus is higher than that in the cortex

Absolute quantitative values for 116 metabolites of the thalamus and cortex in WT and homozygote rats at five weeks are summarized in Supplementary Table 3. PCA (Fig. 6e) and heat map visualization of HCA (Fig. 6f) showed that energy metabolism was different between the two areas in WT rats and the thalamus of homozygote rats compared with the WT. Compound names in the hierarchical cluster analysis are listed in Supplementary Table 3. Table 1 presents a list of metabolites that are statistically increased in the thalamus compared with those in the cortex of WT rats showing an increase in most of the central energy metabolites. On the other hand, many of the metabolites in the thalamus of homozygotes were statistically decreased compared with those of WT rats (Table 2). The only metabolite that was increased in the thalamus with a statistically significant difference was alanine (Table 2).

3.8. Txn1-F54L rat generated by genome editing replicates symmetrical vacuolar degeneration in the midbrain

Finally, we conducted reproducibility experiments to confirm whether the *Txn1*-F54L mutation is the sole cause of the F344/NSlc phenotype. Genome editing using CRISPR-Cas9 was used to generate F344/Jcl rats with the *Txn1*- F54L mutation. We placed 5-week-old F344/Jcl *Txn1*-F54L heterozygous rats under 24-h video monitoring and recorded running seizures eight times/24 h (a total of $n = 5$). Running seizures and transition from running to tonic seizures were observed. These seizure symptoms were similar to those observed in *Adem* rats harboring *Txn1*-F54L. The lesions were localized in the thalamus, hypothalamus, and superior and inferior colliculi and were more extensive in homozygous than in heterozygous rats (Fig. 7a and b). The

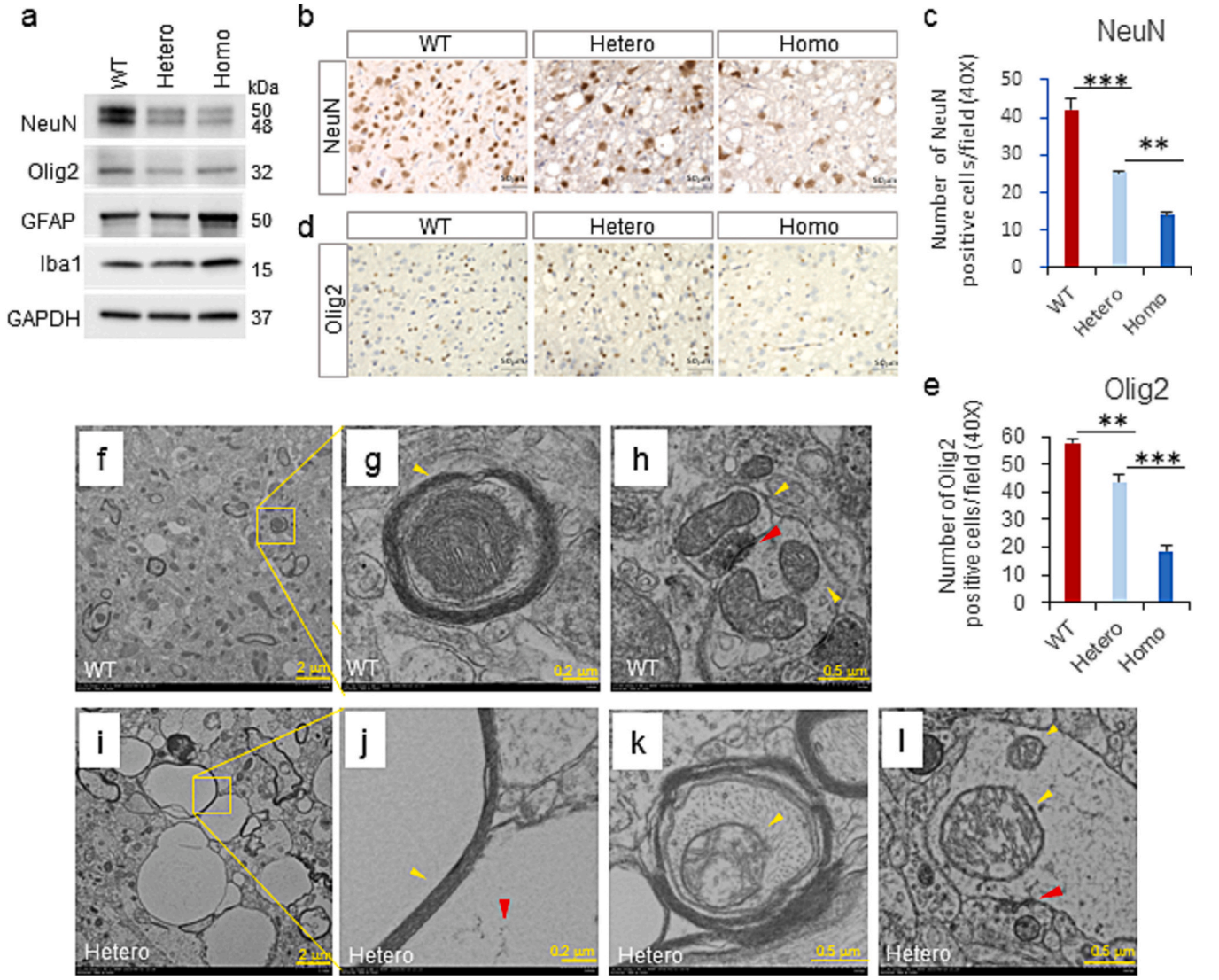

Fig. 4. Neuronal and oligodendrocytic cell loss occurs in the midbrain.
(a) Protein levels of each cell in the midbrain at five weeks. Anti-NeuN, anti-Olig2, anti-GFAP, and Iba1 bodies are markers of neurons, oligodendrocytes, astrocytes, and microglia. This experiment was repeated twice with similar results.
(b) Immunohistochemistry of the anti-NeuN-positive cells in the inferior colliculus for each genotype.
(c) Quantification of NeuN-positive cells. Quantification was performed by assessing five randomly selected fields in the inferior colliculus and thalamus for each genotype.
(d) Immunohistochemistry of Olig2-positive cells in the inferior colliculus for each genotype.
(e) Quantification of Olig2-positive cells. Quantification was performed by assessing five randomly selected fields in the inferior colliculus and thalamus for each genotype.
(f) Representative TEM image in the inferior colliculus of WT rat at four weeks.
(g) Magnification of the axon in (f). The yellow arrowhead indicates myelin sheath.
(h) Representative TEM image of the synapse in the inferior colliculus of WT rat at four weeks. The yellow arrowhead indicates mitochondria with normal morphology, and the red arrowhead indicates postsynaptic density, corresponding with the synaptic terminal.
(i) Representative TEM image of the inferior colliculus of a heterozygous rat at four weeks.
(j) Magnification of the vacuole in (i). The yellow arrowhead indicates the myelin sheath, and the red arrowhead indicates a microtubule.
(k) Representative TEM image of the axon in the midbrain of the heterozygous rat at four weeks. The yellow arrowhead indicates mitochondria with sparse cristae.
(l) Representative TEM image of the synapse in the inferior colliculus of WT rat at four weeks. The yellow arrowhead indicates mitochondria with sparse cristae, and the red arrowhead indicates postsynaptic density. (For interpretation of the references to colour in this figure legend, the reader is referred to the web version of this article.)

vacuoles in the midbrain started developing at two weeks of age, became apparent at three weeks, and recovered at nine weeks (Supplementary Fig. 4). Although the genetic background of F344/NSlc generated by ENU-mutagenesis and F344/Jcl is somewhat different, transient vacuolar degeneration localized in the midbrain was reproduced in F344/Jcl rats carrying the *Txn1*- F54L mutation.

4. Discussion

The study of *Adem* rats, which began with a forward genetic approach, provided significant neurobiological findings. The *Txn1* mutation is associated with the development of symmetrical vacuolar degeneration in the midbrain of juveniles. The F54L mutation impaired insulin-reducing activity and susceptibility to cell death under oxidative

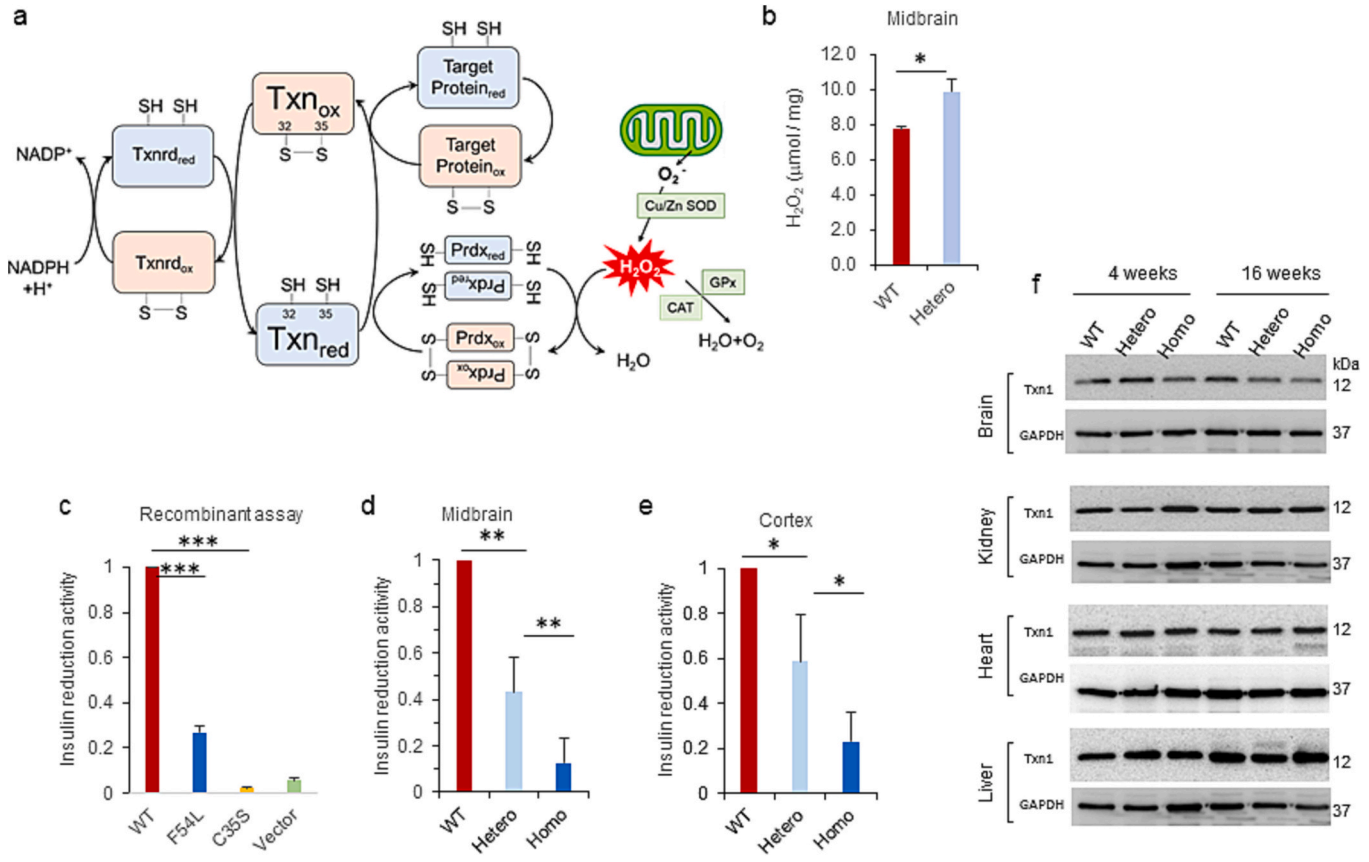

Fig. 5. *Txn1*-F54L shows decreased insulin-reducing activity.
(a) Thioredoxin/peroxiredoxin system.
(b) Concentration of H_2O_2 in the midbrains of WT and heterozygotes.
(c) Insulin-reducing activity determined using recombinant proteins.
(d) Insulin-reducing activity of the midbrain for each genotype.
(e) Insulin-reducing activity of the cortex for each genotype.
(f) Protein level of thioredoxin in the brain, kidney, heart, and liver. This experiment was repeated twice with similar results.

stress. Vacuolar degeneration in the midbrain seems to be linked to running seizures.

4.1. *Txn1-F54L mutation causes characteristic symmetrical vacuolar degeneration in juveniles*

MRI, histological examinations, and a reproducibility experiment using genome editing techniques revealed that the *Txn1* mutation causes bilateral symmetric vacuolar degeneration in the rat midbrain at 3–5 weeks. Western blotting and immunohistochemistry revealed a reduction in the number of neurons and oligodendrocytes in the *Adem* rats. The number of NeuN-positive cells in *Adem* rats was significantly lower than that in the WT, and pronounced axon swelling was identified via TEM. These findings suggest that vacuoles reflect neuronal cells swelling and death. However, this study could not identify which degeneration occurs first, neuronal or oligodendrocytic. Under physiological conditions, neuronal activity controls oligodendrocyte development and myelination (Fields, 2015; Foster et al., 2019); therefore, neuronal cell death can hinder myelination. Inflammatory demyelination and axonal damages cooccur in multiple sclerosis, although their relative roles have been debated (Bitsch et al., 2000; DeLuca et al., 2006). Thus, neurons and oligodendrocytes have reciprocal interactions both physiologically and pathologically (Pease-Raissi and Chan, 2021). When changes are observed simultaneously, it is not easy to determine the dominant one.

Western blotting of five-week-old brains showed a dense band reacting to anti-Iba1 antibody, suggesting an increase in microglia. Microglial activation is a common feature of neurodegenerative diseases. Activated microglia have been reported to kill neurons by releasing TNF-α, glutamate, reactive oxygen, and nitrogen species, which can cause apoptosis, excitotoxicity, and necrotic death of surrounding neurons (Block et al., 2007; Brown and Vilalta, 2015). Therefore, activation of microglia may exacerbate cell death.

4.2. *Txn1-F54L mutation with decreased function is susceptible to cell death under oxidative stress*

Our recombinant protein assay showed that the insulin-reducing activity in the mutant rats decreased to approximately one-third of that of the WT. F54L is located far from the CGPC motif, which plays a central role in thioredoxin activity. The missense mutation may cause a structural change in the region where the dithiol/disulfide exchange reaction occurs.

In primary cultured fibroblasts derived from *Adem* rats, cell death was induced in the culture medium with H_2O_2 more readily than in the WT. In addition, we confirmed a higher concentration of H_2O_2 and stronger staining of IHC with 8-OHdG and 4-HNE in the brain lesions of *Adem* rats than in those of the WT. These results suggest that excessive ROS production in the midbrain lesions of *Adem* rats induced oxidative DNA damage and oxidation of lipids.

Thioredoxin has anti-apoptotic functions in various cells (Andoh et al., 2002; Baker et al., 1997; Haendeler et al., 2002). Loss of thioredoxin function can cause cell death (Benhar, 2020; Circu and Aw,

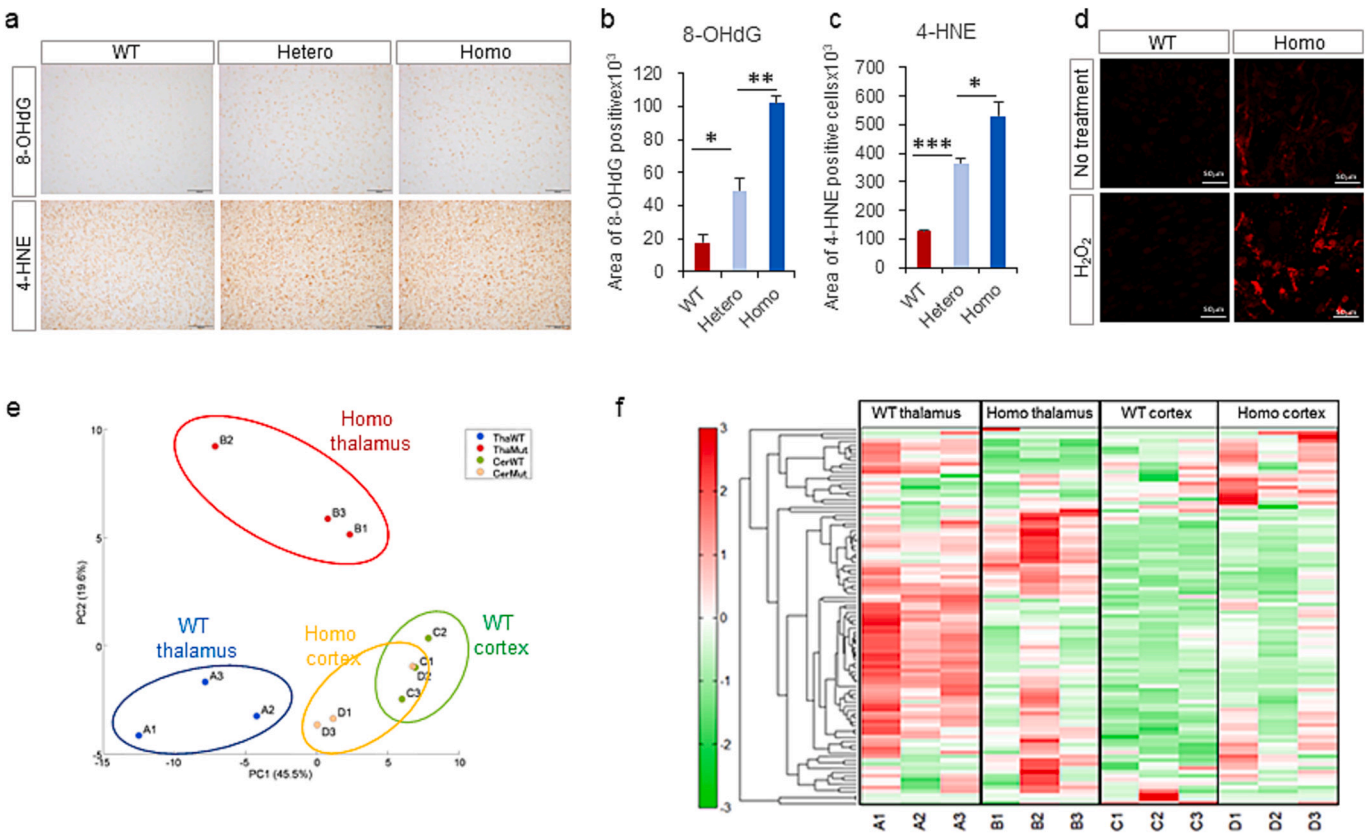

Fig. 6. Oxidative damage in the midbrain and susceptibility to cell death under oxidative stress.
(a) Oxidative damage in the midbrain was assessed by IHC using anti-8-OHdG antibody and 4-HNE.
(b) Quantification of 8-OHdG-positive cells for each genotype.
(c) Quantification of 4-HNE-positive cells for each genotype.
(d) TUNEL assay of the primary fibroblasts derived from the WT and homozygous rats.
(e) Principal component analysis of metabolites of the cerebral cortex and thalamus in WT ($n = 3$) and homozygote (n = 3) rats. The numbers in parentheses indicate the proportion variance of each principal component.
(f) Heat map visualization of the hierarchical cluster analysis of metabolites.

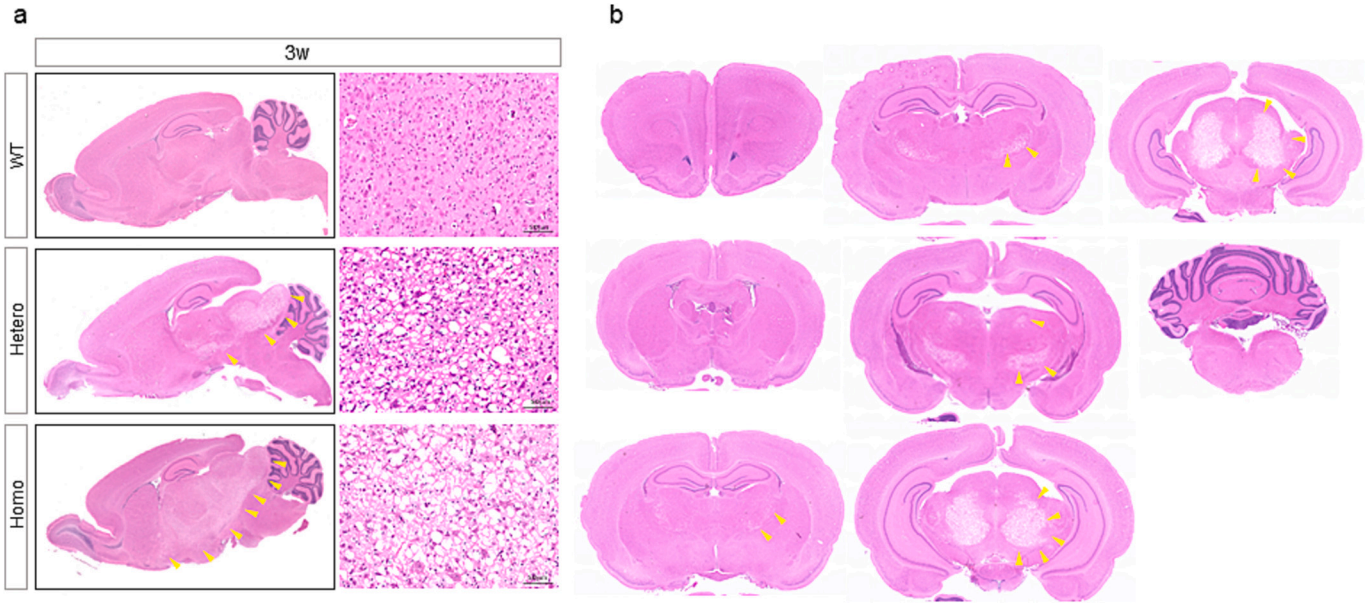

Fig. 7. *Txn1*-F54L rat generated by genome editing replicates the vacuolar degeneration in the midbrain. The yellow arrowheads indicate vacuolar degeneration.
(a) Representative HE staining of the sagittal brain section at three weeks for each genotype.
(b) The coronal slices of the brain for each 500 mm section in the heterozygote. (For interpretation of the references to colour in this figure legend, the reader is referred to the web version of this article.)

Table 1
List of statistically increased metabolites for thalamus vs. cortex in WT rats.

Comparative analysis in WT rats		
Compound name	Thalamus vs. Cortex	
	Ratio	*p*-value
Cystathionine	8.4	0.001
Spermidine	5.5	0.010
Hydroxyproline	5.3	0.006
Ornithine	3.9	0.002
Glycine	3.9	4.2E-05
Uric acid	3.7	0.043
Putrescine	3.5	0.002
Fructose 6-phosphate	3.3	0.003
Carnitine	3.2	0.015
Proline	2.8	0.008
Lysine	2.7	0.003
Dihydroxyacetone phosphate	2.3	0.005
Fumaric acid	2.7	0.013
Betaine	2.5	0.024
Pheylalanine	2.1	0.004
Histidine	2.0	0.008
Tyrosine	2.0	0.018
S-Adenosylmethionine	2.0	0.022
Leucine	1.9	4.4E-04
Isoleucine	1.6	0.001
γ-Aminobutyric acid	1.9	0.040
Citrulline	1.9	0.025
Threonine	1.8	0.031
2-Hydroxyglutaric acid	1.8	0.038
Arginine	1.8	0.008
Aspartic acid	1.8	0.015
ADP	1.8	0.041
Homoserine	1.8	0.035
UDP-glucose	1.6	0.029
Trptophan	1.7	0.010
Methionine	1.7	0.048
NAD^+	1.7	0.018
Asparagine	1.6	0.013
Lactic acid	1.6	0.006
CoA	1.5	0.020
Valine	1.5	0.033
Serine	1.5	0.039
$NADP^+$	1.5	0.021
Succinic acid	1.4	0.026
N-Acetylglutamic acid	1.4	0.042

Ratio = Thalamus/Cortex.

Table 2
List of statistically decreased or increased metabolites for homozygotes vs. WT rats in the thalamus.

Comparative analysis in the thalamus		
Compound name	Homozygotes vs. WT	
	Ratio	*p*-value
Hydroxyproline	0.2	0.003
Glutathione (GSH)	0.2	0.003
Serine	0.4	0.008
Cystathionine	0.4	0.045
Histidine	0.5	0.008
Ornithine	0.5	0.023
Tyrosine	0.5	0.011
NAD^+	0.5	0.007
Carnitine	0.5	0.036
Fructose 6-phosphate	0.6	0.014
Pheylalanine	0.6	0.012
UDP-glucose	0.6	0.030
Asparagine	0.6	0.023
Homoserine	0.6	0.035
Glutamine	0.6	0.025
S-Adenosylmethionine	0.6	0.030
Aspartic acid	0.7	0.045
$NADP^+$	0.7	0.031
AMP	0.7	0.031
β-Alanine	1.6	0.028

Ratio = Homozygotes/WT.

2010; Tonissen and Di Trapani, 2009). Proteins that are associated with apoptosis through the interaction with thioedoxin include apoptosis signal-regulating kinase 1 (ASK1) (Saitoh et al., 1998; Tobiume et al., 2001) and Caspase-3 (CASP3) (Mitchell and Marletta, 2005). Thioredoxin interacts with various proteins, and thioredoxin-interacting protein (TXNIP) is one of the most well-studied proteins with essential functions in vivo. TXNIP is a physiological inhibitor of thioredoxin, and TXNIP activates the NLRP3 inflammasome and leads to apoptosis (Lerner et al., 2012; Oslowski et al., 2012). Moreover, mTOR is an interacting protein of thioredoxin (Oka et al., 2017). mTOR inhibitors have been reported to cause brain tumor cell death via the TXNIP/thioredoxin antioxidant pathway (Malone et al., 2017). Thus, inhibition of thioredoxin leads to cell death, either directly or indirectly, through an interacting protein. In addition to apoptosis, other mechanisms of neuronal death could be involved, such as phagocytosis, pyroptosis, and ferroptosis (Fricker et al., 2018).

4.3. Midbrain lesions and running seizures

As a symptom of epileptic seizures, running seizures were reported mainly in the 1980s and 1990s. Electrical stimulation of the inferior colliculus and midbrain reticular formation (Hirsch et al., 1993; Maton et al., 1997; McCown et al., 1984) or intense acoustic stimulation (Marescaux et al., 1987) induced running seizures. In addition, some evoked running seizures are followed by tonic seizures (Hirsch et al., 1993; Marescaux et al., 1987; Maton et al., 1997). The seizures in the *Adem* rats share similarities with these symptoms. The time of spontaneous appearance and suppression of epileptic seizures and the time of onset and repair of the midbrain lesions were almost the same. This suggests that running seizures in *Adem* rats are linked to midbrain lesions involving the inferior colliculus and thalamus. Due to the lack of EEG analysis, it has not been possible to determine whether this is an epileptic phenomenon. We performed simultaneous video-EEG monitoring for a long term after this study. However, because of severe body movements during the running seizures, we ultimately could not confirm EEG changes during the seizures. However, we found that absence seizures, tonic seizures, and partial seizures appeared during periods of frequent running seizures. We have reported these findings in another publication (Ohmori et al., 2022).

4.4. Dysfunction of the Txn/ Txnrd and Txn/ Prdx systems and related phenotypes

The function of thioredoxin in vivo remains unclear. Herein, we discovered a link between *Txn1* mutations and CNS disorders in mammals for the first time. thioredoxin is located in the cytoplasm, nucleus, and extracellular region (Kang et al., 2019; Rubartelli et al., 1992), whereas thioredoxin-2 (*Txn2*) is located in the mitochondria (Spyrou et al., 1997). A homozygous *Txn2* mutation has been linked to an infantile-onset neurodegenerative disorder with severe cerebellar and optic atrophy and peripheral neuropathy (Holzerova et al., 2016). To our knowledge, there are no reports of *Txn*1 mutations that cause human diseases to date.

Txnrd catalyzes the reduction of oxidized TXN in an NADPH-dependent manner. Genetically modified mice with inactivation of Txnrd1 or Txnrd2 show embryonic lethality (Conrad et al., 2004; Jakupoglu et al., 2005), so the Txn/ Txnrd systems are essential for fetal development. Other important interacting proteins include the Prdx family, which scavenges H_2O_2. Knockout mice for *Prdx1*, *Prdx2*, *Prdx3*, *Prdx4*, or *Prdx5* exhibited various disorders, such as hemolytic anemia, metabolic abnormalities, inflammation, cancer, and age-related phenotypes (Lee, 2020). The discovery of *Adem* rats may shed light on new roles of the Txn/ Txnrd and Txn/ Prdx systems.

4.5. Why is symmetrical vacuolar degeneration confined to the midbrain?

An interesting phenomenon in *Adem* rats is the appearance of bilateral symmetrical lesions in the midbrain at 3–5 weeks. Several experiments failed to explain why vacuolar degeneration is localized to the midbrain. First, western blotting showed that thioredoxin was expressed in several organs other than the brain of *Adem* rats. The thioredoxin is ubiquitously expressed throughout the body (*TXN* thioredoxin [*Homo sapiens* (human)] - Gene - NCBI https://www.ncbi.nlm.nih.gov/gene/7295). Second, the insulin-reducing activity of thioredoxin in *Adem* rats was reduced to one-third of that in the WT, both in the thalamus, where vacuolar degeneration appeared and in the cerebral cortex, where vacuolar degeneration was not present. Third, primary cultured fibroblasts derived from *Adem* rats showed cell death induced by excessive ROS. These results in vitro indicate that cell death can be caused by excessive ROS, regardless of the cell type. The thioredoxin/peroxiredoxin system, not the glutathione system, was reported to significantly contribute to mitochondrial H_2O_2 removal in the brain (Drechsel and Patel, 2010). This may partially explain why degeneration occurs in the brain. However, it does not explain why degeneration does not occur in the cortex but only in the thalamus. Lastly, we wondered if the location-specific microenvironment contributed to the limited onset of neuronal death in the midbrain. The results of the metabolome analysis showed that energy metabolism was higher in the thalamus than in the cortex. The neurodevelopmental stage at 3–5 weeks of age might have an increased mitochondrial ROS leakage due to high energy metabolism in the midbrain. Because the number of rats for metabolome analysis was small, we must interpret it cautiously. However, we must consider another possibility, namely that the F54L mutation impairs an essential midbrain protein, the oxidative-reductive state of which is regulated by thioredoxin. Thioredoxin interacts with a wide variety of proteins (Daloso et al., 2015; Fu et al., 2013; Kumar et al., 2004), but we have only identified the impairment of insulin-reducing activity. The specific proteins reduced by TXN1-F54L have not yet been identified, representing a limitation of this study.

4.6. The future challenge of elucidating repair mechanisms

Another surprising phenomenon in *Adem* rats is that repair of the vacuolar lesions can already be seen at seven weeks on MRI, and they are almost entirely repaired in nine weeks. Both astrocytes and microglia have been reported to be involved in cytotoxicity and tissue repair. Astrocytes have long been thought to inhibit neuronal repair, but it has been noted that glial activation induces neurogenesis and acts in repair (Rolls et al., 2009; Silver and Miller, 2004). Microglia phagocytose debris and dead neurons releasing BDNF and IGF to repair damaged neurons (Bohlen et al., 2019; Colonna and Butovsky, 2017; Nayak et al., 2014). In vacuolar lesions, glial cells with opposing effects may coexist, or switch roles from damage to repair. Although this is an exciting point, it is far from the purpose of this study, which was to identify a causative gene of running seizures and clarify the underlying pathology. We will study this in the future.

4.7. Application of Adem rats in neuroscience research

Oxidative stress is responsible for many neurodegenerative diseases (Elfawy and Das, 2019; Lin and Beal, 2006; Uttara et al., 2009) and cerebral ischemic-reperfusion injury (Allen and Bayraktutan, 2009; Orellana-Urzúa et al., 2020). New therapeutic agents for oxidative stress-related diseases can be evaluated more easily because neuronal death occurs spontaneously in a short time and does not require surgical treatment. For this purpose, *Adem* rats could be attractive animal models.

5. Conclusions

The underlying pathology of *Adem* rats with *Txn1*-F54L mutation is the loss of neurons and oligodendrocytes in the midbrain. In comparison to the WT, these mutants have a decreased insulin-reducing activity. Primary cultured fibroblasts derived from *Adem* rats exhibited cell death under excess H_2O_2. The mutation might affect the midbrain microenvironment in a specific manner, leading to the death of neurons and oligodendrocytes in that region. Further studies are required to determine this midbrain-specific function of TXN1.

Supplementary data to this article can be found online at https://doi.org/10.1016/j.nbd.2022.105921.

Author contributions

T.M discovered the *Adem* rat; I.O. and M.O. performed the phenotypic characterization of this strain; T.M. and S.I. created the genome-edited mutant rats; H.I. supervised the MRI examination and analyzed the data; S.T. supervised the histopathological experiments; Conceptualization, I.O., M.O., and T. M.; Investigation, I.O., M.O., H.I., S.I., S.T., and T.M.; Writing – Original Draft, I.O.; Writing – Review & Editing, M. O. H.I., S.I., S.T., and T. M.; Project Administration, I.O.; Funding Acquisition, I.O., M.O., and T.M. All authors approved the final manuscript.

Funding

This work was supported by Grants-in-Aid for Scientific Research (16H05354 and 22K07914), a Grant-in-Aid for epilepsy research from the Japan Epilepsy Research Foundation, and JSPS KAKENHI Grant Number JP16H06276 (AdAMS).

Declaration of Competing Interest

The authors declare that there are no competing financial interests.

Data availability

No data was used for the research described in the article.

Acknowledgments

We thank Ms. Yumiko Morishita, Mika Monobe, and Miki Kajino for technical assistance with histology and IHC. We thank Ms. Masumi Hurutani for the technical assistance with EM. We would like to thank Editage (www.editage.com) for English language editing.

References

Allen, C.L., Bayraktutan, U., 2009. Oxidative stress and its role in the pathogenesis of ischaemic stroke. Int. J. Stroke 4, 461–470. https://doi.org/10.1111/j.1747-4949.2009.00387.x.

Andoh, T., Chock, P.B., Chiueh, C.C., 2002. The roles of thioredoxin in protection against oxidative stress-induced apoptosis in SH-SY5Y cells. J. Biol. Chem. 277, 9655–9660. https://doi.org/10.1074/jbc.M110701200.

Baker, A., Payne, C.M., Briehl, M.M., Powis, G., 1997. Thioredoxin, a gene found overexpressed in human cancer, inhibits apoptosis *in vitro* and *in vivo*. Cancer Res. 57, 5162–5167.

Benhar, M., 2020. Oxidants, antioxidants and thiol redox switches in the control of regulated cell death pathways. Antioxidants (Basel). 9, 309. https://doi.org/10.3390/antiox9040309.

Bitsch, A., Schuchardt, J., Bunkowski, S., Kuhlmann, T., Brück, W., 2000. Acute axonal injury in multiple sclerosis. Correlation with demyelination and inflammation. Brain. 123, 1174–1183. https://doi.org/10.1093/brain/123.6.1174.

Block, M.L., Zecca, L., Hong, J.S., 2007. Microglia-mediated neurotoxicity: uncovering the molecular mechanisms. Nat. Rev. Neurosci. 8, 57–69. https://doi.org/10.1038/nrn2038.

Bohlen, C.J., Friedman, B.A., Dejanovic, B., Sheng, M., 2019. Microglia in brain development, homeostasis, and neurodegeneration. Annu. Rev. Genet. 53, 263–288. https://doi.org/10.1146/annurev-genet-112618-043515.

Brown, G.C., Vilalta, A., 2015. How microglia kill neurons. Brain Res. 1628, 288–297. https://doi.org/10.1016/j.brainres.2015.08.031.
Circu, M.L., Aw, T.Y., 2010. Reactive oxygen species, cellular redox systems, and apoptosis. Free Radic. Biol. Med. 48, 749–762. https://doi.org/10.1016/j.freeradbiomed.2009.12.022.
Colonna, M., Butovsky, O., 2017. Microglia function in the central nervous system during health and neurodegeneration. Annu. Rev. Immunol. 35, 441–468. https://doi.org/10.1146/annurev-immunol-051116-052358.
Conrad, M., Jakupoglu, C., Moreno, S.G., Lippl, S., Banjac, A., Schneider, M., Beck, H., Hatzopoulos, A.K., Just, U., Sinowatz, F., Schmahl, W., Chien, K.R., Wurst, W., Bornkamm, G.W., Brielmeier, M., 2004. Essential role for mitochondrial thioredoxin reductase in hematopoiesis, heart development, and heart function. Mol. Cell. Biol. 24, 9414–9423. https://doi.org/10.1128/MCB.24.21.9414-9423.2004.
Daloso, D.M., Müller, K., Obata, T., Florian, A., Tohge, T., Bottcher, A., Riondet, C., Bariat, L., Carrari, F., Nunes-Nesi, A., Buchanan, B.B., Reichheld, J.P., Araújo, W.L., Fernie, A.R., 2015. Thioredoxin, a master regulator of the tricarboxylic acid cycle in plant mitochondria. Proc. Natl. Acad. Sci. U. S. A. 112, E1392–E1400. https://doi.org/10.1073/pnas.1424840112.
Dan Dunn, J., Alvarez, L.A., Zhang, X., Soldati, T., 2015. Reactive oxygen species and mitochondria: a nexus of cellular homeostasis. Redox Biol. 6, 472–485. https://doi.org/10.1016/j.redox.2015.09.005.
DeLuca, G.C., Williams, K., Evangelou, N., Ebers, G.C., Esiri, M.M., 2006. The contribution of demyelination to axonal loss in multiple sclerosis. Brain. 129, 1507–1516. https://doi.org/10.1093/brain/awl074.
Drechsel, D.A., Patel, M., 2010. Respiration-dependent H2O2 removal in brain mitochondria via the thioredoxin/peroxiredoxin system. J. Biol. Chem. 285, 27850–27858. https://doi.org/10.1074/jbc.M110.101196.
Dringen, R., 2000. Metabolism and functions of glutathione in brain. Prog. Neurobiol. 62, 649–671. https://doi.org/10.1016/s0301-0082(99)00060-x.
Dröge, W., 2002. Free radicals in the physiological control of cell function. Physiol. Rev. 82, 47–95. https://doi.org/10.1152/physrev.00018.2001.
Elfawy, H.A., Das, B., 2019. Crosstalk between mitochondrial dysfunction, oxidative stress, and age related neurodegenerative disease: etiologies and therapeutic strategies. Life Sci. 218, 165–184. https://doi.org/10.1016/j.lfs.2018.12.029.
Eren, I., Naziroğlu, M., Demirdaş, A., Celik, O., Uğuz, A.C., Altunbaşak, A., Ozmen, I., Uz, E., 2007. Venlafaxine modulates depression-induced oxidative stress in brain and medulla of rat. Neurochem. Res. 32, 497–505. https://doi.org/10.1007/s11064-006-9258-9.
Fields, R.D., 2015. A new mechanism of nervous system plasticity: activity-dependent myelination. Nat. Rev. Neurosci. 16, 756–767. https://doi.org/10.1038/nrn4023.
Forlenza, M.J., Miller, G.E., 2006. Increased serum levels of 8-hydroxy-2′-deoxyguanosine in clinical depression. Psychosom. Med. 68, 1–7. https://doi.org/10.1097/01.psy.0000195780.37277.2a.
Foster, A.Y., Bujalka, H., Emery, B., 2019. Axoglial interactions in myelin plasticity: evaluating the relationship between neuronal activity and oligodendrocyte dynamics. Glia. 67, 2038–2049. https://doi.org/10.1002/glia.23629.
Fricker, M., Tolkovsky, A.M., Borutaite, V., Coleman, M., Brown, G.C., 2018. Neuronal cell death. Physiol. Rev. 98, 813–880. https://doi.org/10.1152/physrev.00011.2017.
Fu, C., Liu, T., Parrott, A.M., Li, H., 2013. Identification of thioredoxin target protein networks in cardiac tissues of a transgenic mouse. Methods Mol. Biol. 1005, 181–197. https://doi.org/10.1007/978-1-62703-386-2_15.
Gysin, R., Kraftsik, R., Sandell, J., Bovet, P., Chappuis, C., Conus, P., Deppen, P., Preisig, M., Ruiz, V., Steullet, P., Tosic, M., Werge, T., Cuénod, M., Do, K.Q., 2007. Impaired glutathione synthesis in schizophrenia: convergent genetic and functional evidence. Proc. Natl. Acad. Sci. U. S. A. 104, 16621–16626. https://doi.org/10.1073/pnas.0706778104.
Haendeler, J., Hoffmann, J., Tischler, V., Berk, B.C., Zeiher, A.M., Dimmeler, S., 2002. Redox regulatory and anti-apoptotic functions of thioredoxin depend on S-nitrosylation at cysteine 69. Nat. Cell Biol. 4, 743–749. https://doi.org/10.1038/ncb851.
Hirota, K., Matsui, M., Iwata, S., Nishiyama, A., Mori, K., Yodoi, J., 1997. AP-1 transcriptional activity is regulated by a direct association between thioredoxin and Ref-1. Proc. Natl. Acad. Sci. U. S. A. 94, 3633–3638. https://doi.org/10.1073/pnas.94.8.3633.
Hirsch, E., Maton, B., Vergnes, M., Depaulis, A., Marescaux, C., 1993. Reciprocal positive transfer between kindling of audiogenic seizures and electrical kindling of inferior colliculus. Epilepsy Res. 15, 133–139. https://doi.org/10.1016/0920-1211(93)90093-m.
Holzerova, E., Danhauser, K., Haack, T.B., Kremer, L.S., Melcher, M., Ingold, I., Kobayashi, S., Terrile, C., Wolf, P., Schaper, J., Mayatepek, E., Baertling, F., Friedmann Angeli, J.P., Conrad, M., Strom, T.M., Meitinger, T., Prokisch, H., Distelmaier, F., 2016. Human thioredoxin 2 deficiency impairs mitochondrial redox homeostasis and causes early-onset neurodegeneration. Brain. 139, 346–354. https://doi.org/10.1093/brain/awv350.
Hovatta, I., Tennant, R.S., Helton, R., Marr, R.A., Singer, O., Redwine, J.M., Ellison, J.A., Schadt, E.E., Verma, I.M., Lockhart, D.J., Barlow, C., 2005. Glyoxalase 1 and glutathione reductase 1 regulate anxiety in mice. Nature. 438, 662–666. https://doi.org/10.1038/nature04250.
Ishida, S., Sakamoto, Y., Nishio, T., Baulac, S., Kuwamura, M., Ohno, Y., Takizawa, A., Kaneko, S., Serikawa, T., Mashimo, T., 2012. Kcna1-mutant rats dominantly display myokymia, neuromyotonia and spontaneous epileptic seizures. Brain Res. 1435, 154–166. https://doi.org/10.1016/j.brainres.2011.11.023.
Jakupoglu, C., Przemeck, G.K., Schneider, M., Moreno, S.G., Mayr, N., Hatzopoulos, A.K., de Angelis, M.H., Wurst, W., Bornkamm, G.W., Brielmeier, M., Conrad, M., 2005. Cytoplasmic thioredoxin reductase is essential for embryogenesis but dispensable for cardiac development. Mol. Cell. Biol. 25, 1980–1988. https://doi.org/10.1128/MCB.25.5.1980-1988.2005.
Kanda, Y., 2013. Investigation of the freely available easy-to-use software 'EZR' for medical statistics. Bone Marrow Transplant. 48, 452–458. https://doi.org/10.1038/bmt.2012.244.
Kang, Z., Qin, T., Zhao, Z., 2019. Thioredoxins and thioredoxin reductase in chloroplasts: a review. Gene. 706, 32–42. https://doi.org/10.1016/j.gene.2019.04.041.
Kumar, J.K., Tabor, S., Richardson, C.C., 2004. Proteomic analysis of thioredoxin-targeted proteins in Escherichia coli. Proc. Natl. Acad. Sci. U. S. A. 101, 3759–3764. https://doi.org/10.1073/pnas.0308701101.
Laurent, T.C., Moore, E.C., Reichard, P., 1964. Enzymatic synthesis of deoxyribonucleotides. IV. J. Biol. Chem. 239, 3436–3444.
Lee, Y.J., 2020. Knockout mouse models for peroxiredoxins. Antioxidants (Basel). 9, 182. https://doi.org/10.3390/antiox9020182.
Lerner, A.G., Upton, J.P., Praveen, P.V., Ghosh, R., Nakagawa, Y., Igbaria, A., Shen, S., Nguyen, V., Backes, B.J., Heiman, M., Heintz, N., Greengard, P., Hui, S., Tang, Q., Trusina, A., Oakes, S.A., Papa, F.R., 2012. IRE1alpha induces thioredoxin-interacting protein to activate the NLRP3 inflammasome and promote programmed cell death under irremediable ER stress. Cell Metab. 16, 250–264. https://doi. https://doi.org/10.1016/j.cmet.2012.07.007.
Lin, M.T., Beal, M.F., 2006. Mitochondrial dysfunction and oxidative stress in neurodegenerative diseases. Nature. 443, 787–795. https://doi.org/10.1038/nature05292.
Lincoln, D.T., Ali Emadi, E.M., Tonissen, K.F., Clarke, F.M., 2003. The thioredoxin-thioredoxin reductase system: over-expression in human cancer. Anticancer Res. 23, 2425–2433.
Lu, J., Holmgren, A., 2014. The thioredoxin antioxidant system. Free Radic. Biol. Med. 66, 75–87. https://doi.org/10.1016/j.freeradbiomed.2013.07.036.
Malone, C.F., Emerson, C., Ingraham, R., Barbosa, W., Guerra, S., Yoon, H., Liu, L.L., Michor, F., Haigis, M., Macleod, K.F., Maertens, O., Cichowski, K., 2017. mTOR and HDAC inhibitors converge on the TXNIP/thioredoxin pathway to cause catastrophic oxidative stress and regression of RAS-driven tumors. Cancer Discov. 7, 1450–1463 (https://doi:10.1158.2159-8290.CD).
Marescaux, C., Vergnes, M., Kiesmann, M., Depaulis, A., Micheletti, G., Warter, J.M., 1987. Kindling of audiogenic seizures in Wistar rats: an EEG study. Exp. Neurol. 97, 160–168. https://doi.org/10.1016/0014-4886(87)90290-1.
Mashimo, T., Yanagihara, K., Tokuda, S., Voigt, B., Takizawa, A., Nakajima, R., Kato, M., Hirabayashi, M., Kuramoto, T., Serikawa, T., 2008. An ENU-induced mutant archive for gene targeting in rats. Nat. Genet. 40, 514–515. https://doi.org/10.1038/ng0508-514.
Maton, B., Vergnes, M., Hirsch, E., Marescaux, C., 1997. Involvement of proprioceptive feedback in brainstem-triggered convulsions. Epilepsia. 38, 509–515. https://doi.org/10.1111/j.1528-1157.1997.tb01133.x.
Matsui, M., Oshima, M., Oshima, H., Takaku, K., Maruyama, T., Yodoi, J., Taketo, M.M., 1996. Early embryonic lethality caused by targeted disruption of the mouse thioredoxin gene. Dev. Biol. 178, 179–185. https://doi.org/10.1006/dbio.1996.0208.
McCown, T.J., Greenwood, R.S., Frye, G.D., Breese, G.R., 1984. Electrically elicited seizures from the inferior colliculus: a potential site for the genesis of epilepsy? Exp. Neurol. 86, 527–542. https://doi.org/10.1016/0014-4886(84)90087-6.
Mitchell, D.A., Marletta, M.A., 2005. Thioredoxin catalyzes the S-nitrosation of the caspase-3 active site cysteine. Nat. Chem. Biol. 1, 154–158. https://doi.org/10.1038/nchembio720.
Miyasaka, Y., Uno, Y., Yoshimi, K., Kunihiro, Y., Yoshimura, T., Tanaka, T., Ishikubo, H., Hiraoka, Y., Takemoto, N., Tanaka, T., Ooguchi, Y., Skehel, P., Aida, T., Takeda, J., Mashimo, T., 2018. CLICK: one-step generation of conditional knockout mice. BMC Genomics 19, 318. https://doi.org/10.1186/s12864-018-4713-y.
Nathan, C., Cunningham-Bussel, A., 2013. Beyond oxidative stress: an immunologist's guide to reactive oxygen species. Nat. Rev. Immunol. 13, 349–361. https://doi.org/10.1038/nri3423.
Nayak, D., Roth, T.L., McGavern, D.B., 2014. Microglia development and function. Annu. Rev. Immunol. 32, 367–402. https://doi.org/10.1146/annurev-immunol-032713-120240.
Ng, F., Berk, M., Dean, O., Bush, A.I., 2008. Oxidative stress in psychiatric disorders: evidence base and therapeutic implications. Int. J. Neuropsychopharmacol. 11, 851–876. https://doi.org/10.1017/S1461145707008401.
Ohashi, Y., Hirayama, A., Ishikawa, T., Nakamura, S., Shimizu, K., Ueno, Y., Tomita, M., Soga, T., 2008. Depiction of metabolome changes in histidine-starved Escherichia coli by CE-TOFMS. Mol. BioSyst. 4, 135–147. https://doi.org/10.1039/b714176a.
Ohmori, I., Ouchida, M., Shinohara, M., Kobayashi, K., Ishida, S., Mashimo, T., 2022. Novel animal model of combined generalized and focal epilepsy. Epilepsia. 63, e80–e85. https://doi.org/10.1111/epi.17295.
Oka, S.I., Hirata, T., Suzuki, W., Naito, D., Chen, Y., Chin, A., Yaginuma, H., Saito, T., Nagarajan, N., Zhai, P., Bhat, S., Schesing, K., Shao, D., Hirabayashi, Y., Yodoi, J., Sciarretta, S., Sadoshima, J., 2017. Thioredoxin-1 maintains mechanistic target of rapamycin (mTOR) function during oxidative stress in cardiomyocytes. J. Biol. Chem. 292, 18988–19000. https://doi.org/10.1074/jbc.M117.807735.
Orellana-Urzúa, S., Rojas, I., Líbano, L., Rodrigo, R., 2020. Pathophysiology of ischemic stroke: role of oxidative stress. Curr. Pharm. Des. 26, 4246–4260. https://doi.org/10.2174/1381612826666200708133912.
Oslowski, C.M., Hara, T., O'Sullivan-Murphy, B., Kanekura, K., Lu, S., Hara, M., Ishigaki, S., Zhu, L.J., Hayashi, E., Hui, S.T., Greiner, D., Kaufman, R.J., Bortell, R., Urano, F., 2012. Thioredoxin-interacting protein mediates ER stress-induced beta cell death through initiation of the inflammasome. Cell Metab. 16, 265–273. https://doi.org/10.1016/j.cmet.2012.07.005.

Pease-Raissi, S.E., Chan, J.R., 2021. Building a (w)rapport between neurons and oligodendroglia: reciprocal interactions underlying adaptive myelination. Neuron. 109, 1258–1273. https://doi.org/10.1016/j.neuron.2021.02.003.

Rolls, A., Shechter, R., Schwartz, M., 2009. The bright side of the glial scar in CNS repair. Nat. Rev. Neurosci. 10, 235–241. https://doi.org/10.1038/nrn2591.

Rubartelli, A., Bajetto, A., Allavena, G., Wollman, E., Sitia, R., 1992. Secretion of thioredoxin by normal and neoplastic cells through a leaderless secretory pathway. J. Biol. Chem. 267, 24161–24164.

Saadat, M., Mobayen, F., Farrashbandi, H., 2007. Genetic polymorphism of glutathione S-transferase T1: a candidate genetic modifier of individual susceptibility to schizophrenia. Psychiatry Res. 153, 87–91. https://doi.org/10.1016/j.psychres.2006.03.024.

Saitoh, M., Nishitoh, H., Fujii, M., Takeda, K., Tobiume, K., Sawada, Y., Kawabata, M., Miyazono, K., Ichijo, H., 1998. Mammalian thioredoxin is a direct inhibitor of apoptosis signal-regulating kinase (ASK) 1. EMBO J. 17, 2596–2606. https://doi.org/10.1093/emboj/17.9.2596.

Sarniak, A., Lipińska, J., Tytman, K., Lipińska, S., 2016. Endogenous mechanisms of reactive oxygen species (ROS) generation. Postepy Hig Med. Dosw. (Online). 70, 1150–1165. https://doi.org/10.5604/17322693.1224259.

Serikawa, T., Mashimo, T., Takizawa, A., Okajima, R., Maedomari, N., Kumafuji, K., Tagami, F., Neoda, Y., Otsuki, M., Nakanishi, S., Yamasaki, K., Voigt, B., Kuramoto, T., 2009. National BioResource Project-Rat and related activities. Exp. Anim. 58, 333–341. https://doi.org/10.1538/expanim.58.333.

Silver, J., Miller, J.H., 2004. Regeneration beyond the glial scar. Nat. Rev. Neurosci. 5, 146–156. https://doi.org/10.1038/nrn1326.

Spyrou, G., Enmark, E., Miranda-Vizuete, A., Gustafsson, J., 1997. Cloning and expression of a novel mammalian thioredoxin. J. Biol. Chem. 272, 2936–2941. https://doi.org/10.1074/jbc.272.5.2936.

Sugimoto, M., Wong, D.T., Hirayama, A., Soga, T., Tomita, M., 2010. Capillary electrophoresis mass spectrometry-based saliva metabolomics identified oral, breast and pancreatic cancer-specific profiles. Metabolomics. 6, 78–95. https://doi.org/10.1007/s11306-009-0178-y.

Tobiume, K., Matsuzawa, A., Takahashi, T., Nishitoh, H., Morita, K., Takeda, K., Minowa, O., Miyazono, K., Noda, T., Ichijo, H., 2001. ASK1 is required for sustained activations of JNK/p38 MAP kinases and apoptosis. EMBO Rep. 2, 222–228. https://doi.org/10.1093/embo-reports/kve046.

Tonissen, K.F., Di Trapani, G., 2009. Thioredoxin system inhibitors as mediators of apoptosis for cancer therapy. Mol. Nutr. Food Res. 53, 87–103. https://doi.org/10.1002/mnfr.200700492.

Uttara, B., Singh, A.V., Zamboni, P., Mahajan, R.T., 2009. Oxidative stress and neurodegenerative diseases: a review of upstream and downstream antioxidant therapeutic options. Curr. Neuropharmacol. 7, 65–74. https://doi.org/10.2174/157015909787602823.

Wakasugi, N., Tagaya, Y., Wakasugi, H., Mitsui, A., Maeda, M., Yodoi, J., Tursz, T., 1990. Adult T-cell leukemia-derived factor/thioredoxin, produced by both human T-lymphotropic virus type I- and Epstein-Barr virus-transformed lymphocytes, acts as an autocrine growth factor and synergizes with interleukin 1 and interleukin 2. Proc. Natl. Acad. Sci. U. S. A. 87, 8282–8286. https://doi.org/10.1073/pnas.87.21.8282.

Yamamoto, M., Yang, G., Hong, C., Liu, J., Holle, E., Yu, X., Wagner, T., Vatner, S.F., Sadoshima, J., 2003. Inhibition of endogenous thioredoxin in the heart increases oxidative stress and cardiac hypertrophy. J. Clin. Invest. 112, 1395–1406. https://doi.org/10.1172/JCI17700.

Yamamoto, H., Fujimori, T., Sato, H., Ishikawa, G., Kami, K., Ohashi, Y., 2014. Statistical hypothesis testing of factor loading in principal component analysis and its application to metabolite set enrichment analysis. BMC Bioinform. 15, 51. https://doi.org/10.1186/1471-2105-15-51.

Yoshimi, K., Kunihiro, Y., Kaneko, T., Nagahora, H., Voigt, B., Mashimo, T., 2016. ssODN-mediated knock-in with CRISPR-Cas for large genomic regions in zygotes. Nat. Commun. 7, 10431. https://doi.org/10.1038/ncomms10431.